



# F doping and P vacancy engineered FeCoP nanosheets for efficient and stable seawater electrolysis at large current density

Jiawei Zhu<sup>a</sup>, Jingqi Chi<sup>a,\*</sup>, Tong Cui<sup>a,b</sup>, Lili Guo<sup>a,b</sup>, Siqi Wu<sup>a,c</sup>, Bin Li<sup>a</sup>, Jianping Lai<sup>a,b</sup>, Lei Wang<sup>a,b,c,\*\*</sup>

<sup>a</sup> Key Laboratory of Eco-chemical Engineering, Ministry of Education, International Science and Technology Cooperation Base of Eco-chemical Engineering and Green Manufacturing, College of Chemical Engineering, Qingdao University of Science and Technology, Qingdao 266042, PR China

<sup>b</sup> College of Chemistry and Molecular Engineering, Qingdao University of Science and Technology, Qingdao 266042, PR China

<sup>c</sup> College of Environment and Safety Engineering, Qingdao University of Science and Technology, Qingdao 266042, PR China

## ARTICLE INFO

### Keywords:

F doping  
FeCoP nanosheet  
P vacancy  
Seawater splitting  
Large current density

## ABSTRACT

Due to the shortage of global freshwater resources and sufficient seawater resources, electrolysis of seawater has become a research hotspot. However, the presence of chloride ions in seawater greatly hinders the development of seawater electrolysis, therefore, constructing catalyst with high catalytic activity and stability against chloride corrosion is essential for seawater electrolysis. In this work, we synthesize F doped FeP and CoP nanosheets with P vacancies (F-FeCoP<sub>v</sub>@IF) by rapidly molten salt and gas-phase phosphorization strategy, which displays bifunctional activity for HER and OER in alkaline seawater. And the assembled F-FeCoP<sub>v</sub>@IF needs 1.94 V and 1.62 V to drive 1000 mA cm<sup>-2</sup> for overall seawater splitting in alkaline seawater and simulated industrial seawater. And the F-FeCoP<sub>v</sub>@IF has outstanding long-term durability for over 100 h and nearly 100% FE. DFT calculations reveal that F-doping and P vacancies can synergistically modulate the electronic structure of FeCoP, which enable F-FeCoP<sub>v</sub>@IF serve as excellent bifunctional electrocatalyst.

## 1. Introduction

To produce high-purity hydrogen as promising alternative fuels, using renewable energy sources in alkaline electrolyzers provide a feasible strategy for environmental and energy sustainability [1–3]. One of the less-discussed requests of water electrolysis is the availability of highly pure water, which may become a bottleneck for large-scale hydrogen production because of the limited access to freshwater yet wealthy access to abundant seawater [4–6]. However, compared to the water electrolysis in acidic or alkaline pure-water, electrocatalytic HER in seawater is more challenging due to a competitive chlorine evolution reaction (ClER) ( $\text{Cl}^- + 2\text{OH}^- = \text{ClO}^- + \text{H}_2\text{O} + 2\text{e}^-$ ) on the counter electrode side [7,8]. At the same time, the production of highly corrosive hypochlorite byproducts will lead to poisoning and seriously block the active site of precious metal catalyst [9,10]. Considering that the onset potential of OER is only ~490 mV lower than that of ClER in alkaline seawater, Pt-like catalysts with highly active and stable catalyst is urgently needed to drive industrial current density (> 500–1000 mA

cm<sup>-2</sup>) with the overpotential less than 490 mV to avoid ClER. Furthermore, designing highly active bifunctional electrocatalysts for both HER and OER are more demanded for practical application because of the merits of simplified devices and low cost [11–14]. Another challenge in alkaline seawater electrolysis is the formation of insoluble precipitates on the surface of catalyst may poison the active sites, thus hindering its long-term stability. Therefore, constructing active and stable bifunctional catalyst with more exposure of active sites is more demanded [15–17].

Non-noble transition-metal phosphides (TMPs), such as Fe, Ni, and Co-based phosphides [18–20], have emerged as efficient HER electrocatalysts due to their high intrinsic activity, adjustable electronic configuration and components, where the electronegative P in the phosphides can serve as base to seize positively charged H protons, thus boosting its HER activity [21–23]. Recently, attention has been paid to cation doped-phosphides, involving Mo-Ni<sub>3</sub>S<sub>2</sub>/Ni<sub>x</sub>P<sub>y</sub> [24], Fe-Co<sub>2</sub>P BNRs [25] and Ru/Ni-CoP [26], to further enhance the HER activity due to its chemical advantages and tunable structure [27]. Compared with

\* Corresponding author.

\*\* Corresponding author at: Key Laboratory of Eco-chemical Engineering, Ministry of Education, International Science and Technology Cooperation Base of Eco-chemical Engineering and Green Manufacturing, College of Chemical Engineering, Qingdao University of Science and Technology, Qingdao 266042, PR China.

E-mail addresses: [chijingqi@qust.edu.cn](mailto:chijingqi@qust.edu.cn) (J. Chi), [inorchemwl@126.com](mailto:inorchemwl@126.com) (L. Wang).

<https://doi.org/10.1016/j.apcatb.2023.122487>

Received 25 August 2022; Received in revised form 11 January 2023; Accepted 18 February 2023

Available online 19 February 2023

0926-3373/© 2023 Elsevier B.V. All rights reserved.

the different cationic doping, anionic fluorine with the strongest electronegativity owns its unique advantage, which can form strong ionic metal-fluorine bonds, thus will be easily dissociated in the alkaline media and facilitate the anion exchange between the F and OH ions, beneficial for the formation of active metal (hydro)oxide phase [28]. Moreover, anion vacancies such as P, S, and O vacancies [29], have been explored for electrocatalytic process, because their advantages of modifying electronic structures of catalyst would balance the adsorption and desorption of intermediates. However, constructing anion vacancy still faces challenges due to their high formation energies and relatively difficult synthesis method [30].

In light of the above inspiration, F doping densely packed FeP and CoP nanosheets with P vacancies (F-FeCoP<sub>v</sub>@IF) have been fabricated via fast molten ammonium fluoride and hydrate cobalt nitrate, and then subsequent phosphorization process. DFT results demonstrate the coexistence of fluorination and P vacancies tune the electronic structure of FeCoP, which can serve as outstanding bifunctional catalyst for HER and OER in alkaline seawater. The as-prepared F-FeCoP<sub>v</sub>@IF demands the low overpotentials of only 210 mV and 370 mV to drive large current density of 1000 mA cm<sup>-2</sup>. Excitingly, the assembled F-FeCoP<sub>v</sub>@IF requires an ultra-low voltage of 1.90 V and 1.59 V to drive 1000 mA cm<sup>-2</sup> as both the anode and cathode for OWS in room condition (25 °C and 1.0 M KOH) and simulated industrial conditions (60 °C and 6.0 M KOH), respectively, and with excellent long-term durability for more than 100 h and almost 100% Faradaic efficiency. Combination of experimental and theoretical results demonstrate that F dopants act as electron-withdrawing atoms to modulate the surface charge distribution, and the P vacancies brings the d-band center closer to the Fermi level, which enable F-FeCoP<sub>v</sub>@IF to have excellent bifunctional activity in alkaline seawater.

## 2. Experimental section

### 2.1. Chemical and materials

Cobalt nitrate hexahydrate (Co(NO<sub>3</sub>)<sub>2</sub> · 6 H<sub>2</sub>O), Ammonium fluoride (NH<sub>4</sub>F), sodium hypophosphite (NaH<sub>2</sub>PO<sub>2</sub>), potassium hydroxide (KOH), sodium chloride (NaCl), ethanol, acetone, deionized water, commercial Pt/C (20%), RuO<sub>2</sub>, iron foam (IF) (1.5 mm in thickness).

### 2.2. Synthesis of F-FeCoO@IF precursor

The F-FeCoO@IF electrocatalysts are prepared via a facile molten method. In advance of preparation, a piece of commercial foam iron (IF) was cut into small pieces of 1 × 2 cm in dimension. The small piece was successively cleaned by sonication with dilute hydrochloric acid (0.1 M), acetone, and ethanol for 20 min, in order to remove the contaminants and impurities on the surface of IF. Finally, the cleaned IF was dried in a vacuum oven for the subsequent experiments. First of all, 10 g Co(NO<sub>3</sub>)<sub>2</sub> · 6 H<sub>2</sub>O and 0.55 g NH<sub>4</sub>F were placed in a glass bottle, and reacted at 100 °C until obtain the molten mixture. Subsequently, the pretreated IF was put into the molten mixture for an ultrafast time of only 5 min. The obtained F-FeCoO@IF was obtained after rinsing with deionized water and drying.

### 2.3. Synthesis of F-FeCoP<sub>v</sub>@IF catalyst

The F-FeCoO@IF and NaH<sub>2</sub>PO<sub>2</sub> (1.0 g) in porcelain boats were treated at 350 °C for 2 h at a rate of 2 °C min<sup>-1</sup> under the Ar atmosphere, and then cooled down to 25 °C to obtain F-FeCoP<sub>v</sub>@IF with a loading of about 5.0 mg cm<sup>-2</sup>.

### 2.4. Synthesis of FeCoO@IF and FeCoP<sub>v</sub>@IF control samples

The FeCoO@IF was synthesized with the same process as F-FeCoO@IF, except that NH<sub>4</sub>F is not added. And the synthesis process of

FeCoP<sub>v</sub>@IF was the same with that of F-FeCoP<sub>v</sub>@IF by replacing the F-FeCoO@IF with FeCoO@IF.

### 2.5. Synthesis of F-FeCoO@IF-0 and F-FeCoP<sub>v</sub>@IF-1.5 control samples

The synthesis process of F-FeCoO@IF-0 and F-FeCoP<sub>v</sub>@IF-1.5 were the same as that of F-FeCoP<sub>v</sub>@IF, except that the amount of NaH<sub>2</sub>PO<sub>2</sub> used in the phosphorization process was 0 g and 1.5 g, respectively.

### 2.6. Synthesis of Pt/C and RuO<sub>2</sub> catalysts on IF

For comparison with typical benchmarks, commercial Pt/C catalyst (5 mg) was dispersed in a mixed solution containing deionized water, ethanol, and Nafion, respectively, and their volume ratio was 25:23:2, followed by sonication for 20 min to form a uniform catalyst ink. Then, the catalyst ink was dropped into clean IF and air-dried overnight at room temperature to obtain IF-supported Pt/C electrodes. RuO<sub>2</sub> electrodes was also synthesized by the similar method. The loading capacity of the precious metal catalyst prepared by this method is about 5.0 mg cm<sup>-2</sup>.

### 2.7. Materials characterizations

The composition and phase structure of the catalyst were verified by X-ray diffraction (XRD) (X'Pert PRO MPD) at a scan rate of 5° min<sup>-1</sup>, and 2θ range of 5 ~ 90°. Scanning electron microscopy (SEM) (Hitachi S-8200), transmission electron microscopy (TEM) (JEM-2100UHR), and TEM elemental mapping were used in this experiment to analyze the microstructure, morphology, and element distribution of the samples. Electron paramagnetic resonance (EPR) (Bruker A300 Germany) spectroscopy was used to detect the presence of phosphorus vacancies. The atomic composition and chemical valence state of the sample surface were obtained by X-ray photoelectron spectroscopy (XPS) using a monochromatic Al K<sub>α</sub> source (15 mA and 14 kV). During the processing, the C 1 s value was set to 284.6 eV for charge correction.

### 2.8. Electrochemical measurement

All electrochemical measurements were performed on a Gamry Reference 3000 electrochemical workstation. A graphite rod and saturated calomel electrode (SCE) were used as the counter and reference electrode, respectively. As-prepared catalyst supported on iron foam was used as working electrode. The relevant potential in this experiment was calculated using the following formula for the reversible hydrogen electrode (RHE): E(RHE) = E(SCE) + 0.243 V + 0.059 pH. HER and OER tests were performed in 1.0 M KOH, 1 M KOH + 0.5 M NaCl, and 1.0 M KOH + seawater solutions. Linear scan voltammetry (LSV) polarization curves for OER and HER were obtained at a scan rate of 5 mV s<sup>-1</sup>. Electrochemical impedance spectroscopy (EIS) was measured in the frequency range from 0.01 to 10<sup>5</sup> Hz. To measure the electrochemically active surface area, CV cycling at different scan rates (40–120 mV s<sup>-1</sup>) were carried out. Long-term stability tests were performed by chronoamperometry i-t test at 25 °C and 60 °C.

### 2.9. Simulation methods

The current first principle DFT calculations are obtained by Vienna Ab initio Simulation Package (VASP) [31] and the projector augmented Wave (PAW) means [32]. The exchange relation functional is treated by employing the generalized gradient approximation (GGA) of Perdew-Burke-Ernzerhof (PBE) functional [33]. The energy cession for the plane wave basis proliferation was set to 450 eV and the strength on each atom less than 0.03 eV/Å was set for convergence criterion of geometry relaxation. Grimme's DFT-D3 method was applied to depict dispersion interactions. Incomplete occupancies of the Kohn–Sham orbitals were permitted using the Gaussian smearing measure and a width

of 0.05 eV [34]. Throughout the calculation, the Brijulin section was sampled with a Monkhorst grid of  $3 \times 3 \times 1$ . The self-consistent calculations apply a convergence energy threshold of  $10^{-5}$  eV. To refrain interactions between two adjacent images, a 15 Å vacuum space along the z direction was supplemented. The adsorption of hydrogen on surface was calculated as follows:  $\Delta G_{H^*} = E(\text{slab} + H^*) - E(\text{slab}) - 1/2E(H_2) + \Delta E(\text{ZPE}) - T\Delta S$ , Where  $E(\text{slab} + H^*)$  is the total energy for the adsorption  $H$ , and  $E(\text{slab})$  is the energy of pure surface, and  $E(H_2)$  is the energy of  $H_2$  in gas phase.  $\Delta E(\text{ZPE})$  is the zero-point energy change and  $\Delta S$  is the entropy change. the Gibbs free energy calculation was corrected by a constant of 0.24 eV at 298 K as:  $\Delta G_{H^*} = E(\text{slab} + H^*) - E(\text{slab}) - 1/2E(H_2) + 0.24$ .

### 3. Results and discussion

#### 3.1. Synthesis and characterization of F-FeCoP<sub>v</sub>@IF nanosheets

The F doping densely packed FeCoP nanosheets with P vacancies are synthesized via a two-step process, as indicated in Fig. 1a. Firstly, the F-FeCoO@IF nanosheets are in-situ grown on iron foam (IF) through an ultrafast molten method using the molten salt mixture of  $\text{Co}(\text{NO}_3)_2 \cdot 6\text{H}_2\text{O}$  and  $\text{NH}_4\text{F}$  (Fig. S1a), where the  $\text{NH}_4\text{F}$  serve as morphology-guiding agent to enable the formation of nanosheet-like structure. This innovative method ensures the formation of rich active sites with high-density and homogeneous distribution. Then the final F-FeCoP<sub>v</sub>@IF product with P vacancies are obtained after phosphorization in an inert atmosphere. Fig. 1b exhibits the SEM image of F-FeCoP<sub>v</sub>@IF, which can be noted that a large amount of ultrathin nanosheets are intertwined to form the nanoflowers. The nanoflower-like structure can not only

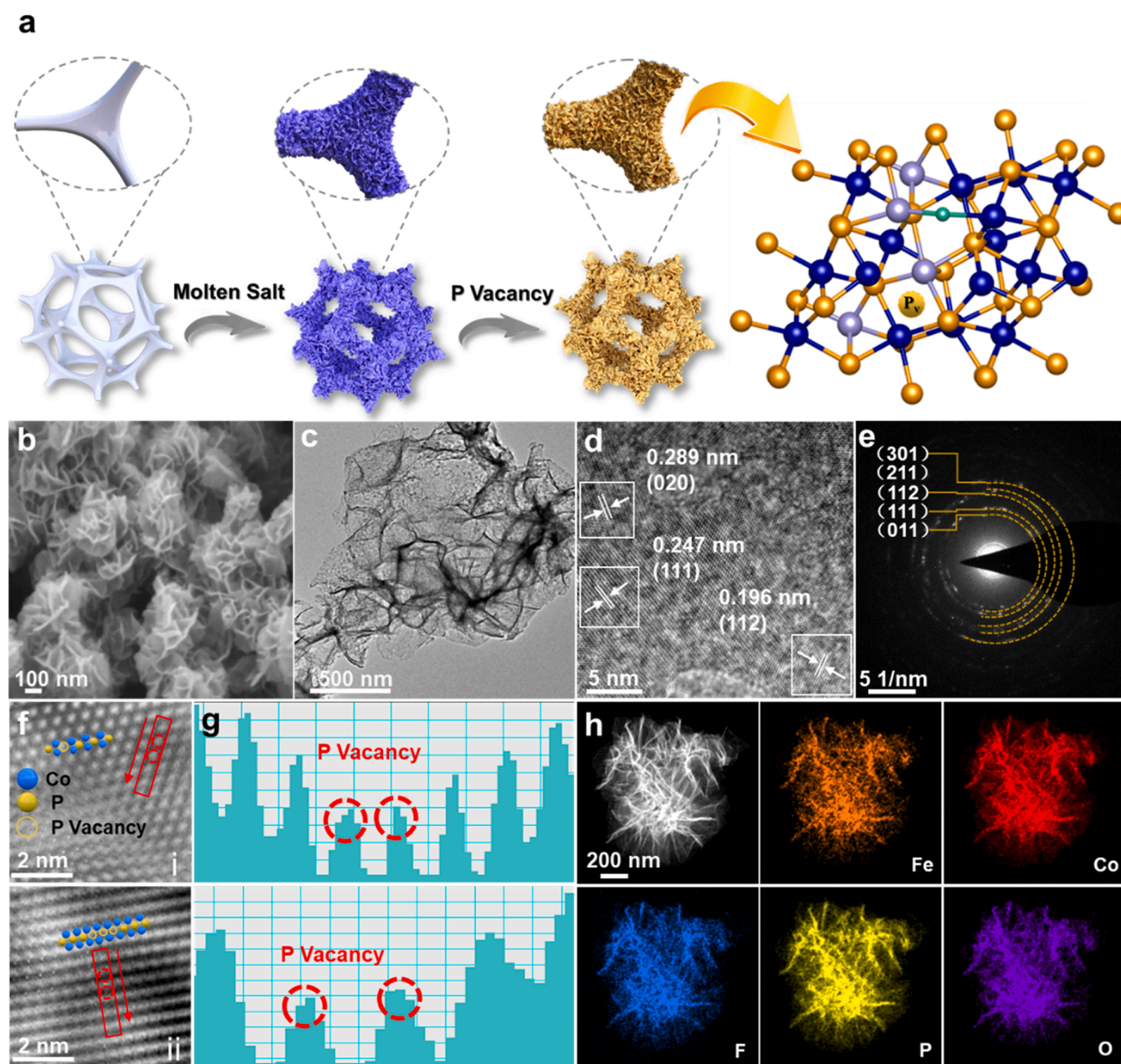


**Fig. 1.** (a) Schematic exemplification of the synthesis procedure for F-FeCoP<sub>v</sub>@IF. (b) SEM, (c) TEM, (d) HRTEM image, and (e) typical SAED pattern of F-FeCoP<sub>v</sub>@IF. (f) HRTEM images and (g) Intensity profile of corresponding areas in Fig. 1f. (h) TEM and TEM mapping image of F-FeCoP<sub>v</sub>@IF.



provide massive surface area with plentiful active sites for water electrolysis, but also expedite electrolyte dispersion and bubble release. Meanwhile, to further explore the effect of  $\text{NH}_4\text{F}$  on the morphology, SEM images of  $\text{FeCoO@IF}$  and  $\text{FeCoP}_v\text{@IF}$  without  $\text{NH}_4\text{F}$  are presented. As observed in Fig. S1b and S1c, the as-prepared  $\text{FeCoO@IF}$  and  $\text{FeCoP}_v\text{@IF}$  are composed of large amount of particles with severe stacking, which indicates that  $\text{NH}_4\text{F}$  plays an essential role in forming the nanosheet-like structure. TEM image of  $\text{F-FeCoP}_v\text{@IF}$  further reveals that the  $\text{F-FeCoP}_v\text{@IF}$  are composed of ultrathin 2D nanosheets with many folds on the surface (Fig. 1c). The HRTEM images reveals that the observed lattice fringes with a spacing of 0.196 nm and 0.247 nm can be assigned to the (112) and (111) planes of CoP (PDF#29-0497), while the lattice fringes with a spacing of 0.289 nm are assigned to the (020) plane of FeP (PDF#39-0809) (Fig. 1d). In addition, the corresponding HRTEM image of  $\text{F-FeCoO@IF}$  displays the crystal distance of 0.248 nm, corresponding to (111) plane of FeO crystal structure (Fig. S2). The diffraction rings pointing to CoP observed using the selective electron diffraction (SAED) pattern of  $\text{F-FeCoP}_v\text{@IF}$  are consistent with the HRTEM results, which implies that FeCoP is the main phase of  $\text{F-FeCoP}_v\text{@IF}$  (Fig. 1e). Consequently, the existence of P vacancies in the  $\text{F-FeCoP}_v\text{@IF}$  catalyst was probed by the Fourier transform and inverse Fourier transform of high-resolution transmission electron microscopy.

As indicated by red circles in Fig. 1f, anionic P vacancies can be observed in the HRTEM images [35]. The intensity profiles (Fig. 1g) of the framed fields in Fig. 1f further confirm the existence of P vacancies of  $\text{F-FeCoP}_v\text{@IF}$  catalyst. Moreover, the EDS mappings of  $\text{F-FeCoP}_v\text{@IF}$  (Fig. 1h) exhibits the homogeneous distribution of Fe, Co, F, P, and O elements throughout the whole nanosheets, which implies that F element is successfully doped into FeCoP structure.

Moreover, the crystal structure and chemical state of the samples were further analyzed by XRD and XPS. Fig. 2a illustrates the XRD patterns of  $\text{F-FeCoP}_v\text{@IF}$  with peaks at  $31.7^\circ$ ,  $46.3^\circ$ ,  $48.1^\circ$ ,  $52.3^\circ$  and  $56.8^\circ$  corresponding to the (011), (112), (211) (103) and (301) crystallographic planes of CoP (PDF#29-0497) and peaks at  $34.5^\circ$ ,  $45.5^\circ$  and  $48.3^\circ$  corresponding to the (200), (201) and (211) crystal planes of FeP (PDF#29-0497), indicating that the main crystalline phase of  $\text{F-FeCoP}_v\text{@IF}$  is FeCoP. Other diffraction peaks at  $44.6^\circ$ ,  $65^\circ$ , and  $82.3^\circ$  correspond to the (110), (200), and (211) crystal planes of Fe substrate (PDF#06-0696). Meanwhile, the XRD patterns of  $\text{F-FeCoO@IF}$ ,  $\text{FeCoO@IF}$ , and  $\text{FeCoP}_v\text{@IF}$  are performed in Fig. S3, which reveals that

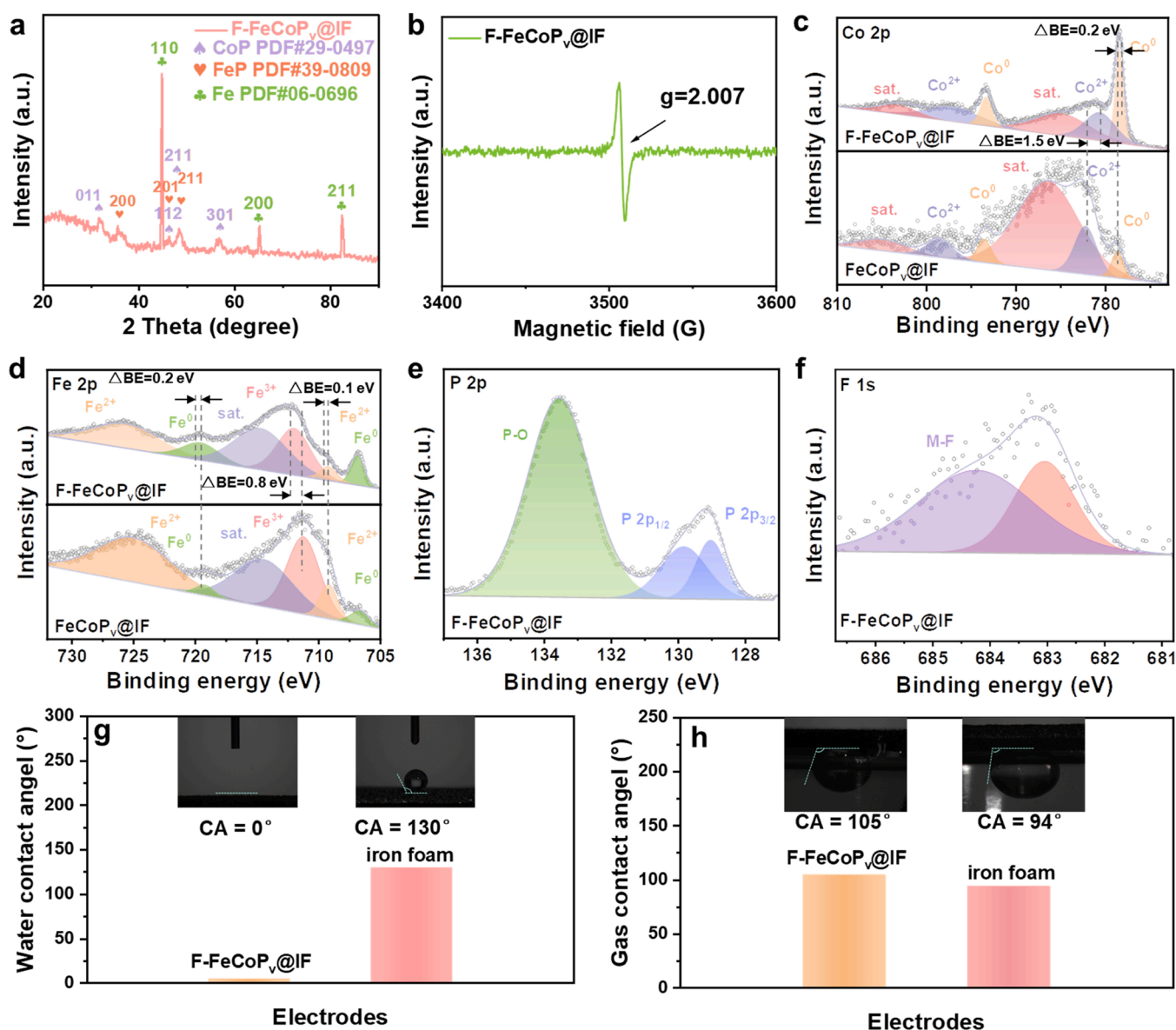
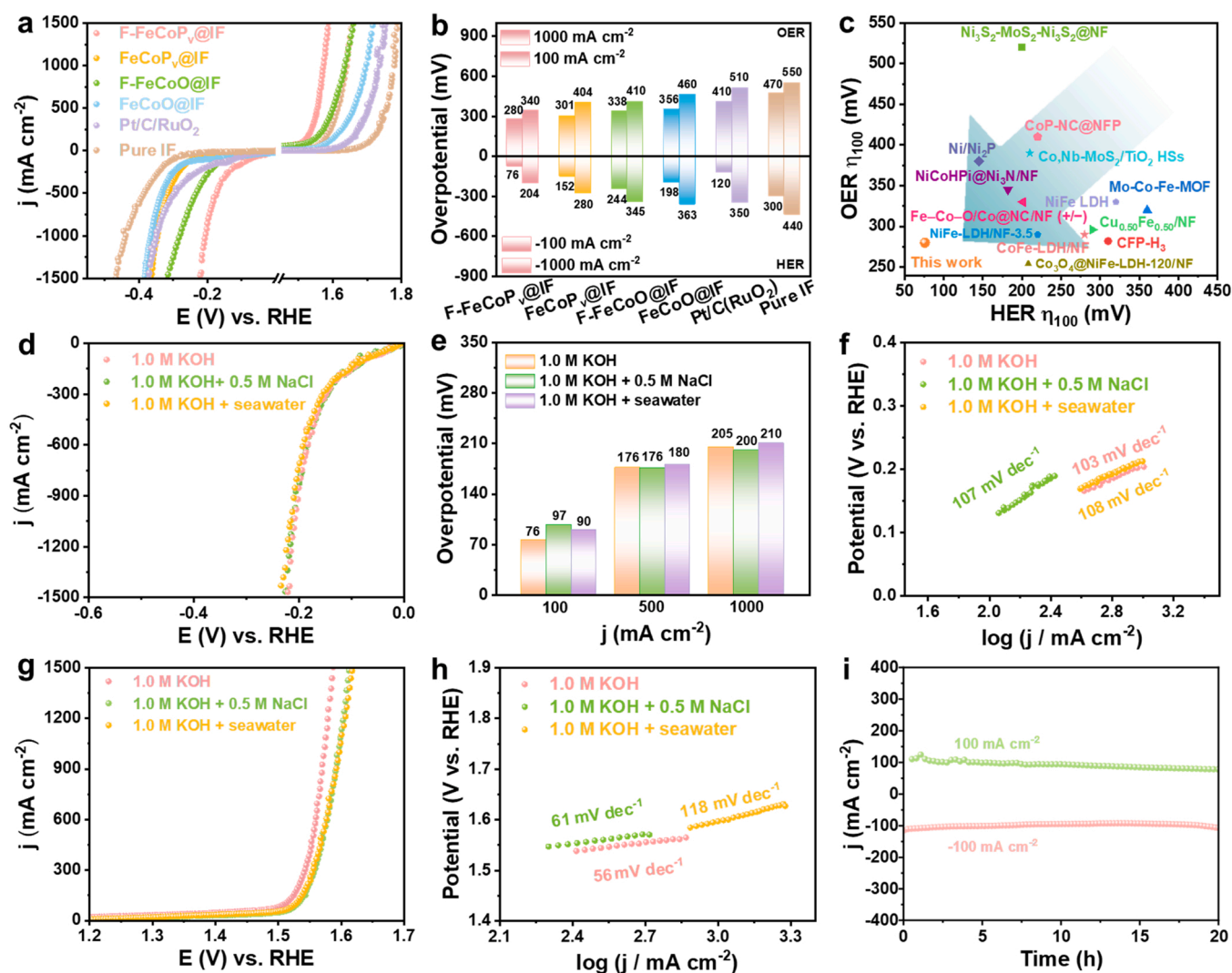


Fig. 2. (a) XRD pattern and (b) EPR spectra of  $\text{F-FeCoP}_v\text{@IF}$ . (c-f) XPS spectra of  $\text{F-FeCoP}_v\text{@IF}$  and  $\text{F-FeCoO@IF}$ , including Co 2p, Fe 2p, P 2p, and F 1s signal. (g, h) Photos of contact angle measurements of bare IF and  $\text{F-FeCoP}_v\text{@IF}$ .



the main phase of the F-FeCoO@IF and FeCoO@IF are FeO (PDF#75-1550) and the main phase of FeCoP<sub>v</sub>@IF is the same as that of F-FeCoP<sub>v</sub>@IF. The above results indicate that the FeCoO@IF precursor is successfully converted into FeCoP during the phosphorization process. Afterward, it is found that phosphorization process with different phosphorization amounts do not cause the transform of FeCoP crystal phase (Fig. S4). To further confirm the specific vacancy type of F-FeCoP<sub>v</sub>@IF, electron paramagnetic resonance (EPR) spectrum of F-FeCoP<sub>v</sub>@IF is displayed in Fig. 2b, where a powerful signal at  $g = 2.007$  is derived from the anion P vacancies [36]. These results indicate that F-FeCoP<sub>v</sub>@IF has high P vacancies formed due to the phosphorization process, which is consistent with the HRTEM results observed in Fig. 1f. Moreover, the EPR with different phosphating amounts reveals that the intensity of P vacancies is positively correlated with the amount of NaH<sub>2</sub>PO<sub>2</sub> during phosphorization process (Fig. S5). The XPS was carried out to gain insights into the surface chemical states and electronic interactions. Fig. 2c displays the high-resolution XPS spectrum of Co 2p, in which two peaks located at 797.1 eV and 780.7 eV are originated from Co<sup>2+</sup>, and the two peaks at 778.4 eV and 793.3 eV correspond to Co<sup>0</sup> [37,38]. The high-resolution XPS spectrum of Fe 2p of F-FeCoP<sub>v</sub>@IF contains two different types of iron species (Fig. 2d), in which two peaks

at 706.7 and 719.6 eV [39] can be attributed to Fe<sup>0</sup> and the higher binding energies at 725.5 and 708.6 eV [40] correspond to the Fe<sup>2+</sup>. Another peak at 712.1 eV is assigned to the Fe<sup>3+</sup>. It can be seen from Figs. 2c and 2d that F doping induces a negative shift of the Co 2p and positive shift of Fe 2p in the FeCoP<sub>v</sub>@IF in comparison with FeCoP<sub>v</sub>@IF, indicating that F doping modulate the electronic structure of metals. By comparing with F-FeCoO@IF, FeCoP is generated in the phosphorization process, which is demonstrated by the appearance of Co-P bonds in the Co 2p of F-FeCoP<sub>v</sub>@IF (Fig. S6). As for the high-resolution XPS spectra of P (Fig. 2e), aside from the oxidation peak for P-O at 133.5 eV, the two peaks corresponding to P 2p<sub>1/2</sub> and P 2p<sub>3/2</sub> can be found at 129.8 and 129.0 eV, respectively [41], which belong to the peak of M-P bond [42]. The high-resolution of F 1s spectra display that the peak at 684.2 eV [43] is consistent with the M-F in the F-FeCoP<sub>v</sub>@IF (Fig. 2f). Then the contact angle (CA) of droplets and gases on F-FeCoP<sub>v</sub>@IF and IF were tested. For the contact angles of droplets on the surfaces of the two samples, CA of 0° for F-FeCoP<sub>v</sub>@IF and CA of 130° for IF indicate that F-FeCoP<sub>v</sub>@IF has excellent hydrophilicity, which can improve the permeability of electrolytes (Fig. 2g). Also, the contact angle of the gas shows a CA of 105° for F-FeCoP<sub>v</sub>@IF and CA of 94° for IF (Fig. 2h). Therefore, F-FeCoP<sub>v</sub>@IF has better gas-repellent performance, which



**Fig. 3.** (a) Electrocatalytic HER and OER performance of F-FeCoP<sub>v</sub>@IF and control samples in 1.0 M KOH. (b) Overpotential of F-FeCoP<sub>v</sub>@IF and control samples at 100 and 1000 mA cm<sup>-2</sup> for HER and OER. (c) Comparison of the overpotential for HER and OER (at 100 mA cm<sup>-2</sup>) of the F-FeCoP<sub>v</sub>@IF with other electrocatalysts. (d) LSV curves, (e) overpotentials at 100, 500, and 1000 mA cm<sup>-2</sup>, (f) corresponding Tafel plots of F-FeCoP<sub>v</sub>@IF for HER in different electrolytes. (g) Polarization curves and (h) corresponding Tafel plots of F-FeCoP<sub>v</sub>@IF for OER in different electrolytes. (i) Chronoamperometry i-t curve of F-FeCoP<sub>v</sub>@IF for HER and OER in alkaline seawater.

can promote the release of bubbles from the surface of F-FeCoP<sub>v</sub>@IF to boost electrochemical reaction rate [44,45].

### 3.2. Investigation of electrocatalytic HER and OER activities

The electrocatalytic performance of F-FeCoP<sub>v</sub>@IF and its control samples for HER and OER in 1.0 M KOH electrolytes are firstly evaluated in a typical three-electrode configuration. As the linear sweep voltammetry (LSV) curves show in Figs. 3a and 3b, F-FeCoP<sub>v</sub>@IF only require a low overpotential of 76 and 280 mV to achieve a large current density of 100 mA cm<sup>-2</sup> for HER and OER, respectively, superior to FeCoP<sub>v</sub>@IF (152 mV and 301 mV), FeCoO@IF (198 mV and 356 mV), F-FeCoO@IF (244 mV and 338 mV), Pt/C/RuO<sub>2</sub> (120 mV and 410 mV) and Pure IF (300 mV and 470 mV). The IR-corrected polarization curve is shown in Fig. S7. And the FeCoP<sub>v</sub>@IF catalyst also has advantages at high current density, which only requires 204 and 340 mV to achieve the large current density of 1000 mA cm<sup>-2</sup> for HER and OER, respectively. It can be concluded that F doping and P vacancies can enhance the performance of HER and OER, which is significant for large-scale H<sub>2</sub> production through water electrolysis. Notably, the HER and OER performance of F-FeCoP<sub>v</sub>@IF has surpassed some recently reported catalysts (Fig. 3c and Table S1). To gain insight into the reaction kinetics, we derive the Tafel slope from the polarization curves associated with the OER/HER kinetics. Fig. S8 displays that the Tafel slope of F-FeCoP<sub>v</sub>@IF is 103 mV and 67 mV dec<sup>-1</sup> for OER and HER, which are smaller than those of that FeCoP<sub>v</sub>@IF (200 and 93 mV dec<sup>-1</sup>), F-FeCoO@IF (109 and 155 mV dec<sup>-1</sup>), FeCoO@IF (111 and 117 mV dec<sup>-1</sup>), Pt/C/RuO<sub>2</sub> (211 and 101 mV dec<sup>-1</sup>), and Pure IF (178 and 133 mV dec<sup>-1</sup>), indicating the accelerated reaction kinetics of F-FeCoP<sub>v</sub>@IF. As shown in Fig. S9, the EIS results show that the F-FeCoP<sub>v</sub>@IF catalyst has the smallest semi-circle among all samples, demonstrating that it has the smallest  $R_{ct}$  value, and further confirm that the remarkable charge transfer kinetics among the HER and OER process. Furthermore, due to that the electrochemical surface area (ECSA) is proportional to the double layer capacitance ( $C_{dl}$ ), so Fig. S10 show the  $C_{dl}$  values calculated by the CV curves tested in the non-Faraday interval, and F-FeCoP<sub>v</sub>@IF with  $C_{dl}$  value of 50.53 mF cm<sup>-2</sup> (Table S2) is the largest among all samples, which imply that F-FeCoP<sub>v</sub>@IF has the largest electrochemically active surface area (Fig. S11), further explaining that F doping FeCoP with P vacancies can provide more active site. In addition, the specific activity (ECSA normalized current density) and turnover frequency (TOF) values were calculated (Fig. S12 and S13), which show that the intrinsic activity of F-FeCoP<sub>v</sub>@IF catalyst exceeds that of the other samples under the same condition. It is suggested that F doping and P vacancy have a positive effect on the improvement of activity. Moreover, the table of TOF values and loadings for the catalysts are exhibited in Table S3, which reveal that F-FeCoP<sub>v</sub>@IF is also significantly better than recently reported catalysts. Considering the excellent catalytic activity of F-FeCoP<sub>v</sub>@IF in 1.0 M KOH, we tested the electrocatalytic performance of F-FeCoP<sub>v</sub>@IF in simulate alkaline seawater (1.0 M KOH + 0.5 M NaCl) and natural alkaline seawater (1.0 M KOH + seawater) electrolytes. Surprisingly, the HER activity of F-FeCoP<sub>v</sub>@IF still sustains high activity with no obvious decay in 1.0 M KOH + 0.5 M NaCl and 1.0 M KOH + seawater (Fig. 3d), only requiring as low as 200 and 210 mV to obtain a current density of 1000 mA cm<sup>-2</sup>, respectively (Fig. 3e). The IR-corrected polarization curve is shown in Fig. S14. At the same time, the measured Tafel slope for F-FeCoP<sub>v</sub>@IF in 1.0 M KOH + 0.5 M NaCl and 1.0 M KOH + seawater are 107 and 108 mV dec<sup>-1</sup> (Fig. 3f). Furthermore, the Nyquist plots confirm that the charge transfer resistance of F-FeCoP<sub>v</sub>@IF in 1.0 M KOH + 0.5 M NaCl and 1.0 M KOH + seawater solutions are similar to that in 1.0 M KOH during HER process (Fig. S15). Fig. 3g and 3h display the LSV curve and Tafel slope of OER in different solutions, respectively. Therefore, the overpotentials of F-FeCoP<sub>v</sub>@IF at 1000 mA cm<sup>-2</sup> are 360 mV, and 370 mV in 1.0 M KOH + 0.5 M NaCl and 1.0 M KOH + seawater solutions, respectively (Fig. S16). The IR-corrected polarization curve is shown in Fig. S17. As

shown in Fig. 3h, the Tafel slope of F-FeCoP<sub>v</sub>@IF are found as 145 mV dec<sup>-1</sup> and 234 mV dec<sup>-1</sup> in alkaline similar to simulated seawater and seawater. The charge transfer resistance of F-FeCoP<sub>v</sub>@IF in 1.0 M KOH + 0.5 M NaCl and 1.0 M KOH + seawater solutions are nearly the same with that in 1.0 M KOH (Fig. S18). Notably, the catalytic activity of F-FeCoP<sub>v</sub>@IF is superior to that of most recently reported catalysts in alkaline seawater (Table S4). In order to explore the effects of different P and F amount on HER and OER properties in different solutions, F-FeCoP<sub>v</sub>@IF series control samples were compared. As shown in Fig. S19 and S20, the HER and OER properties of F-FeCoP<sub>v</sub>@IF in solution were superior to those of other samples, illustrating that appropriate amount of F and P amount with P vacancies can enhance the bifunctional HER and OER activity. Durability is another important property when considering the practical application of catalysts. As shown in Fig. 3i, the current decay of F-FeCoP<sub>v</sub>@IF is negligible and no obvious erosion trace emerge on the electrode surface after 20 h of sustained electrolysis at around 100 mA cm<sup>-2</sup> for HER and OER in alkaline seawater, demonstrating the excellent stability of F-FeCoP<sub>v</sub>@IF catalyst. In addition, ICP measurements were performed to understand the dissolution of various elements after stability tests (Table S5). The contents of Co and Fe in the solution indicate the slight dissolution of these elements. For P element, the relative large percentage of P is dissolved in the solution, especially for OER process, due to the oxidation of P species, which is consistent with the previously reported literature [46]. Afterwards, we further measured the SEM and XPS of F-FeCoP<sub>v</sub>@IF after the stability test. As shown in Fig. S21, the structure of the nanoflowers can still be seen in the SEM images after HER and OER stability tests, which indicates the stability of the nanosheet-like structure. Prominently, as shown in Fig. S22, the intensity of the diffraction peaks of F-FeCoP<sub>v</sub>@IF have been weakened, but the crystal phase structure of CoP can still be observed, which proves the stability of the catalyst. Moreover, the EPR after stability test clearly show that the vacancies signal of P still exist, indicating that the P vacancies is stable before and after the reaction (Fig. S23). The XPS spectra of F-FeCoP<sub>v</sub>@IF after the HER stability test were also carried out. Fig. S24 express the XPS spectra after the HER stability test, where the peaks in the Co 2p and Fe 2p spectra shift to lower binding energy due to the cathodic reduction reaction [45,47]. As displayed in Fig. S25, for P 2p and F 1s spectra after HER, phosphides can still be observed, and the weakening of F peak may be due to the surface dissolution phenomenon of M-F bond during the reaction [48]. After the OER stability test, it can be observed that the XPS of Co and Fe 2p spectra shift to higher binding energy (Fig. S26). It is worth noting that the peak intensity of the Co-P bond becomes weaker, along with the appearance of Co<sup>3+</sup> [49,50]. The Fe 2p spectrum shows that the peak of Fe<sup>0</sup> disappeared, indicating that the Fe<sup>0</sup> is oxidized to Fe<sup>3+</sup> and Fe<sup>2+</sup>. Furthermore, P 2p spectrum show that partial phosphides is oxidized to P-O bond and PO<sub>4</sub><sup>3-</sup> species, and the signal of F spectra became very weak, indicating the leaching of F on the catalyst surface (Fig. S27). The disappearance of the M-F bond may be due to the increase of M-OH/OOH species [51]. Furthermore, the solution values of elements on the catalyst surface before and after the reaction were measured by XPS, as displayed in Table S6. After long-term electrolysis, Ca and Mg elements can be detected by XPS analysis, indicating that trace amount of Ca(OH)<sub>2</sub> and Mg(OH)<sub>2</sub> precipitate on the surface of the sample. Moreover, there are no traces of chlorides on the electrode surface, demonstrating that the chlorine-free HER in alkaline seawater (Fig. S28 and Table S7).

### 3.3. Mechanism for the enhanced HER and OER

To further explore the effect of F doping and P vacancies in F-FeCoP<sub>v</sub>@IF catalysts, the density functional theory (DFT) is calculated according to the feasible structural models (e.g., FeCoP<sub>v</sub>@IF, F-FeCoP@IF and F-FeCoP<sub>v</sub>@IF) indicated in Fig. S29. The motion of the P atom results in the appearance of the P vacancy, and the P vacancy is indicated in the structural models [52,53]. For the construction of the

P-vacancy participation model, we believe that surface vacancies can directly reflect the effect of vacancies on electrochemical reactions compared with internal vacancies, so we choose surface P-vacancies, and also consider that Fe atoms can change the local coordination environment of the original structure more easily to some extent, so P-vacancies will be more likely to be generated near Fe atoms. The Bader charge for three models reveal that these F doping and P vacancies arouse substantial changes in the charge of the adjacent atoms, endowing active sites optimized adsorption of superficial atoms and molecules (Fig. 4a and S30). The differential charge density further indicates that the electron-withdrawing property of F atoms that allow a large number of electrons to be stored nearby (Fig. 4b). Moreover, after the formation of P vacancies, the Co sites will not be enriched with more electrons, which is conducive to the occurrence of subsequent reactions [54]. The density of states (DOS) of F-FeCoP<sub>v</sub>@IF reveal that there are more charges nearby the Fermi level than those of F-FeCoP@IF and FeCoP<sub>v</sub>@IF (Fig. 4c), indicating the enhanced conductivity of F-FeCoP<sub>v</sub>@IF. Moreover, the d-band center of F-FeCoP<sub>v</sub>@IF at  $-0.80$  eV is more close to the Fermi level compared with that of  $-1.38$  eV for FeCoP<sub>v</sub>@IF and  $-0.90$  eV for F-FeCoP@IF, which implies that the adsorption energy of the reactants is further enhanced during the

reaction process. Additionally, the work function in F-FeCoP<sub>v</sub>@IF ( $4.843$  eV) is lower than FeCoP<sub>v</sub>@IF ( $4.903$  eV) and F-FeCoP@IF ( $4.923$  eV) (Fig. 4d and S31), revealing that more electrons are inclined to spill over to the surface of F-FeCoP<sub>v</sub>@IF to participate in electrocatalytic reactions. The adsorption energy of H<sub>2</sub>O on Co and Fe sites were firstly calculated (Fig. 4e). The results show that Co site displays much lower adsorption energy of H<sub>2</sub>O compared with that of Fe site, indicating the fastest H<sub>2</sub>O-adsorption ability, thus beneficial for following water electrolysis. To further explicate the surface construction transformation of F-FeCoP<sub>v</sub>@IF during HER and OER, in-situ Raman spectroscopy at different potentials was conducted. For HER, the spectrum for the as-prepared F-FeCoP<sub>v</sub>@IF displays an obvious peak at  $676\text{ cm}^{-1}$  corresponding to FeCoP species within the measured potential range ( $0\sim-0.4$  V) [55], and no other visible surface change can be observed (Fig. 4f). Then, the H-adsorption free energy ( $\Delta G_{\text{H}^*}$ ) of F-FeCoP<sub>v</sub>@IF and its control samples are calculated (Fig. 4g). The  $\Delta G_{\text{H}^*}$  value of F-FeCoP<sub>v</sub>@IF is the lowest at  $0.228$  eV, which suggests that F doping and P vacancy jointly improve the adsorption/desorption energy of H, there by promoting HER process. For OER, F-FeCoP<sub>v</sub>@IF and FeCoP<sub>v</sub>@IF samples were tested by in-situ Raman (Figs. 4h and 4i). One prominent peak at  $683\text{ cm}^{-1}$  assigned to FeCoOOH species is observed

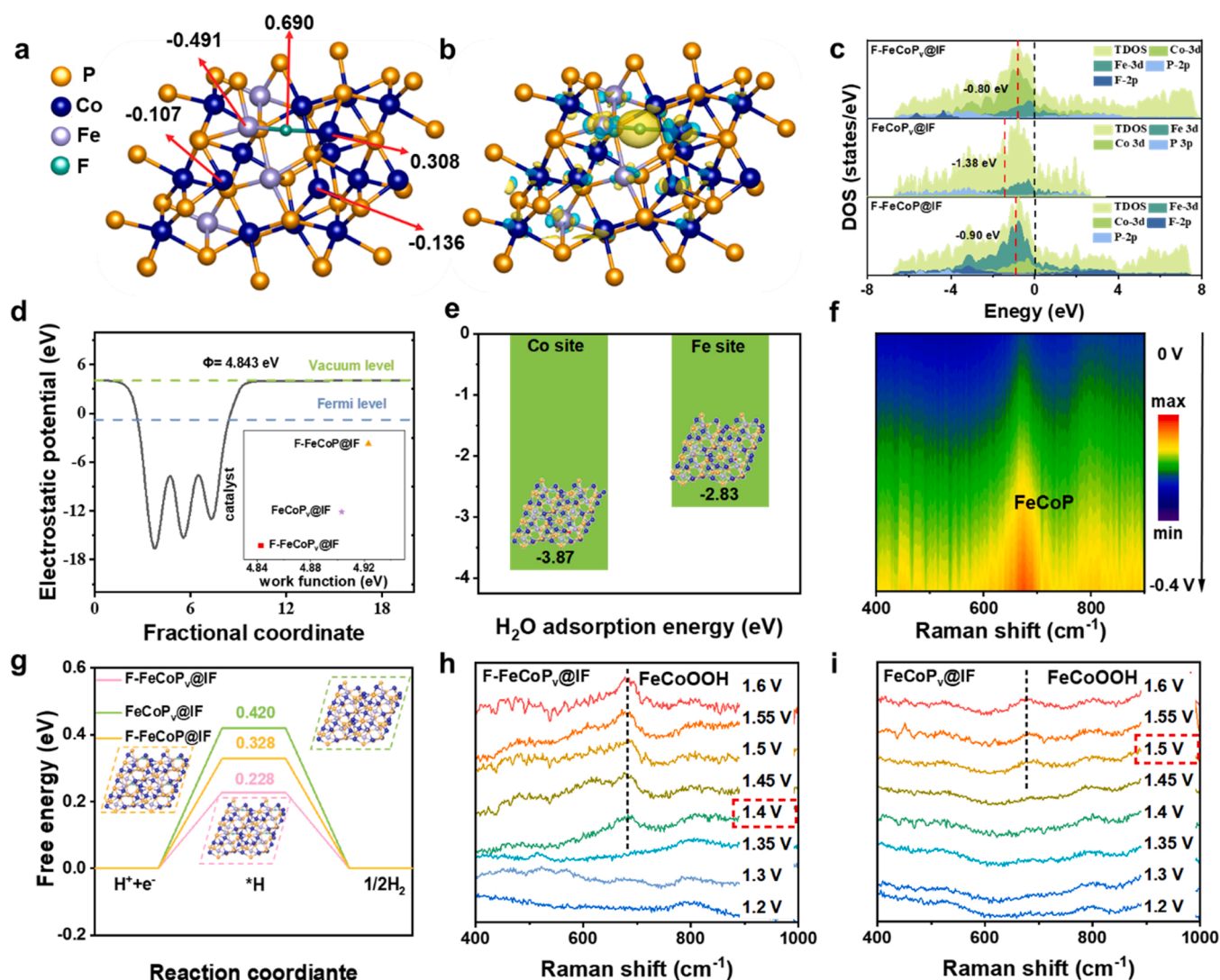


Fig. 4. DFT calculated profiles of F-FeCoP<sub>v</sub>@IF. (a) Bader charge, (b) Charge density difference analysis (blue indicates charge depletion, yellow indicates charge accumulation) of F-FeCoP<sub>v</sub>@IF. (c) DOS of FeCoP<sub>v</sub>@IF, F-FeCoP<sub>v</sub>@IF and F-FeCoP@IF. (d) The computed work functions of F-FeCoP<sub>v</sub>@IF. (e) Diagram of the active site for H<sub>2</sub>O adsorption. (f) In situ Raman of the F-FeCoP<sub>v</sub>@IF sample in HER. (g) H-adsorption energy on different position. In-situ Raman for (h) F-FeCoP<sub>v</sub>@IF and (i) FeCoP<sub>v</sub>@IF in OER.



through the continuous increase of the potential, suggesting that the catalyst undergoes surface reconstruction during the OER process, and the evolved hydroxide species ( $\text{FeCoOOH}$ ) is the real active site for the OER reaction, which is consistent with the previously reported literature [56–58]. In addition, the potential of generating hydroxyl oxide for  $\text{F-FeCoP}_v\text{/IF}$  (1.4 V) is significantly smaller than  $\text{FeCoP}_v\text{/IF}$  (1.5 V), indicating that F doping facilitates the faster conversion of phosphides to hydroxyl oxide, which is beneficial to the improvement of OER activity.

### 3.4. Investigation of electrocatalytic activity for overall seawater splitting

Inspired by the excellent bifunctional electrocatalytic activity of the  $\text{F-FeCoP}_v\text{/IF}$  catalyst in alkaline seawater, the activity of  $\text{F-FeCoP}_v\text{/IF}$  in a two-electrode electrolyzer was measured in 1.0 M KOH (at 25 °C), 1.0 M KOH + seawater (at 25 °C), and simulated industrial electrolysis conditions at 6.0 M KOH (at 60 °C) and 6.0 M KOH + seawater (at 60 °C) solutions. LSV curves of the  $\text{F-FeCoP}_v\text{/IF}$  under 1.0 M KOH + seawater and 6.0 M KOH + seawater at 25 and 60 °C (Fig. 5a). The overpotential for a large current density of  $1000 \text{ mA cm}^{-2}$  requires 1.92 V in 1.0 M KOH + seawater and the overpotential is decreased from 1.92 V to 1.62 V in 6.0 M KOH + seawater due to the quicker interface kinetics, larger driving strength of  $\text{OH}^-$  ions in the solution, and speedier desorption of gas molecules. Notably, the electrochemical activity of  $\text{F-FeCoP}_v\text{/IF}$  in alkaline seawater is superior to those of recently reported catalysts and even exceeds that of commercial Pt/

$\text{C||RuO}_2$  couples (Table S8 and Fig. S32). The IR-corrected polarization curve is shown in Fig. S33. Further, the chronoamperometry i-t curve in 1.0 M KOH + seawater and 6.0 M KOH + seawater solutions can last at least for 100 h without obvious current decay (Fig. 5b). Further enduring stability of seawater splitting is evaluated via chronoamperometry i-t at 100, 300, 600, 900, and 1200  $\text{mA cm}^{-2}$  (Fig. S34), which denotes that  $\text{F-FeCoP}_v\text{/IF}$  catalyst is advantageous for the application of seawater splitting. Thereafter, the Faradaic efficiency of the electrolyzer in 1.0 M KOH + seawater was calculated by the volume of the collected gas (Fig. S35). It can be seen from Figs. 5c and 5d that air bubbles are generated at both the anode and cathode of the electrolytic cell, and the volume of the generated gas can be reflected from the reduction of the liquids. As shown in Fig. 5e, the obtained  $V_{\text{H}_2}/V_{\text{O}_2}$  value is calculated as 2:1, which entails that the catalyst has a Faradaic efficiency of 100% in a 1.0 M KOH + seawater solution. Then, the overall seawater splitting can be actuated by a Stirling engine with innumerable gas bubbles quickly filling the entire balloon (Figs. S36 and 5f). In addition, the OER and HER bifunctional performance of  $\text{F-FeCoP}_v\text{/IF}$  electrocatalyst can also be demonstrated from solar panels powered energy, and it can be noticed that the red balloon is more inflated than the blue balloon, manifesting that the electrolyzer composed of  $\text{F-FeCoP}_v\text{/IF}$  catalyst is more energy-efficient than the commercial  $\text{RuO}_2\text{/Pt/C}$  catalyst (Figs. S37 and 5g). This further confirms the great potential of  $\text{F-FeCoP}_v\text{/IF}$  bifunctional electrocatalyst for large-scale hydrogen production from seawater electrolysis.

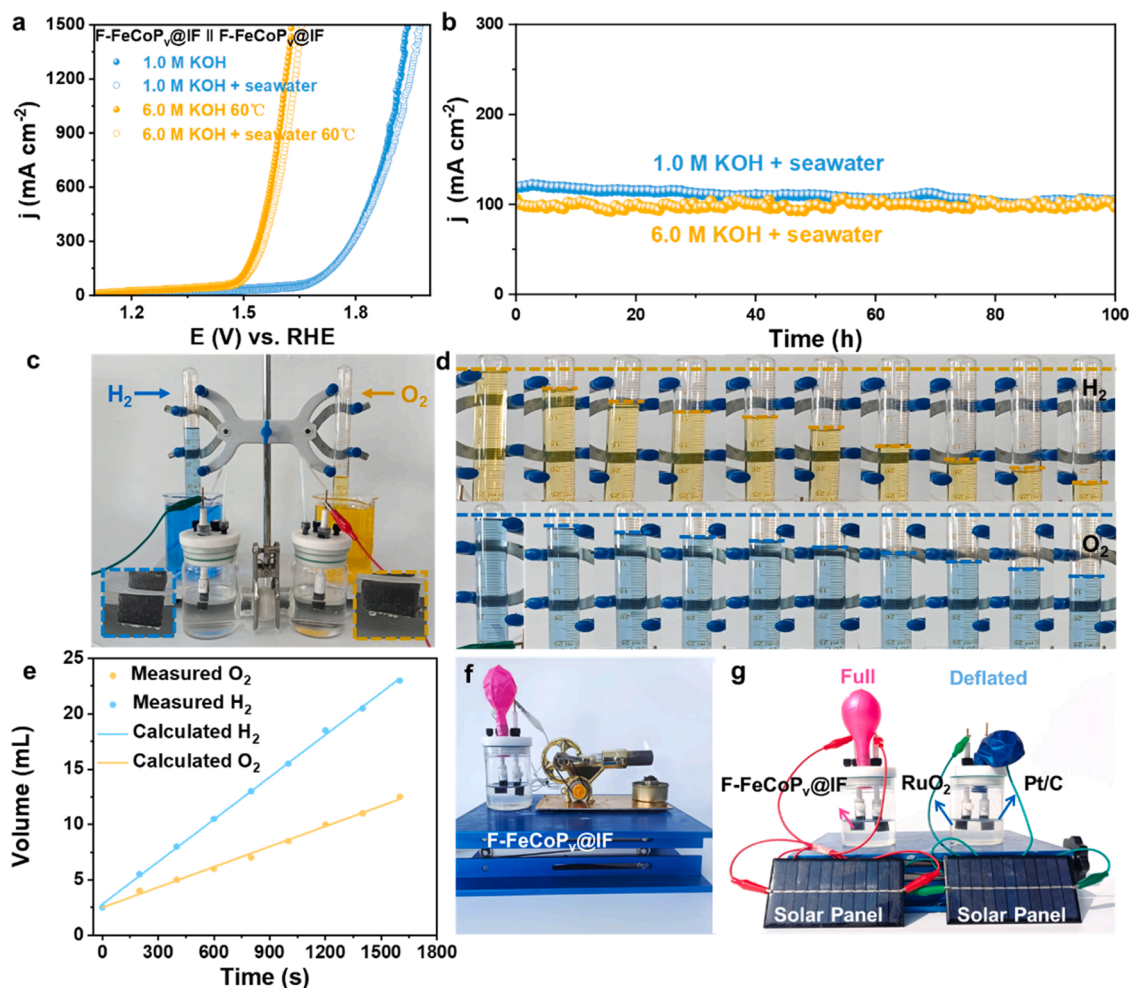


**Fig. 5.** (a) LSV curves in 1.0 M KOH, 1.0 M KOH + seawater, 6.0 M KOH (60 °C), and 6.0 M KOH + seawater (60 °C) for overall water splitting. (b) Chronoamperometry i-t curve of 100 h for  $\text{F-FeCoP}_v\text{/IF}$  in 1.0 M KOH seawater and 6.0 M KOH+ seawater. (c) Photographs of homemade two-electrode cell. (d) Photographs of gases produced at the anode and cathode at different times. (e) The volume of the gas changes with time. Schematic diagram of seawater electrolysis driven by (f) Stirling engine and (g) solar panels.

## 4. Conclusion

In summary, we synthesized F doping densely packed FeCoP nano-sheets with P vacancies (F-FeCoP<sub>v</sub>@IF) by a rapidly molten salt and subsequent phosphorization process, which can be applied as highly active and stable bifunctional HER and OER catalyst in seawater. The catalyst requires only overpotentials of 210 mV and 370 mV to drive a large current density of 1000 mA cm<sup>-2</sup> for HER and OER in alkaline seawater. More importantly, the assembled F-FeCoP<sub>v</sub>@IF has ultra-low voltages of 1.90 V and 1.59 V to drive the 1000 mA cm<sup>-2</sup> at room temperature (25 °C and 1.0 M KOH) and simulated industrial conditions (60 °C and 6.0 M KOH) in the two-electrode cell, and exhibit outstanding stability for over 100 h of continuous operation and nearly 100% FE. DFT calculations reveal that the F doping and P vacancies can synergistically promote the d-band center closer to the Fermi level, which regulate the electronic structure of FeCoP and enhance the adsorption energy of the reactants. This work provides a new direction to modulate the bifunctional electrocatalytic activity in alkaline seawater for large-scale hydrogen production.

## CRediT authorship contribution statement

**Jiawei Zhu:** Investigation, Data curation, Conceptualization, Formal analysis, Validation, Writing – original draft. **Jingqi Chi:** Conceptualization, Writing – review & editing, Supervision, Funding acquisition. **Tong Cui:** Formal analysis, Data curation, Conceptualization, Validation. **Lili Guo:** Data curation, Conceptualization, Validation. **Siqi Wu:** Conceptualization, Validation. **Bin Li:** Supervision, Validation. **Jianping Lai:** Supervision, Validation. **Lei Wang:** Writing – review & editing, Funding acquisition, Supervision.

## Declaration of Competing Interest

The authors declare that they have no known competing financial interests or personal relationships that could have appeared to influence the work reported in this paper.

## Data availability

No data was used for the research described in the article.

## Acknowledgements

This work is financially supported from the National Natural Science Foundation of China (51772162, 52072197, 52174283, and 21971132), Outstanding Youth Foundation of Shandong Province, China (ZR2019JQ14), the Natural Science Foundation of Shandong Province (ZR2021QE165), Youth Innovation and Technology Foundation of Shandong Higher Education Institutions, China (2019KJC004), Major Scientific and Technological Innovation Project (2019JZZY020405), Major Basic Research Program of Natural Science Foundation of Shandong Province under Grant (ZR2020ZD09), and Taishan Scholar Young Talent Program (tsqn201909114).

## Appendix A. Supporting information

Supplementary data associated with this article can be found in the online version at [doi:10.1016/j.apcatb.2023.122487](https://doi.org/10.1016/j.apcatb.2023.122487).

## References

- [1] J.A. Turner, Sustainable hydrogen production, *Science* 305 (2004) 972–974, <https://doi.org/10.1126/science.1103197>.
- [2] H. Nishiyama, T. Yamada, M. Nakabayashi, Y. Maehara, M. Yamaguchi, Y. Kuromiya, Y. Nagatsuma, H. Tokudome, S. Akiyama, T. Watanabe, R. Narushima, S. Okunaka, N. Shibata, T. Takata, T. Hisatomi, K. Domen, Photocatalytic solar hydrogen production from water on a 100-m<sup>2</sup> scale, *Nature* 598 (2021) 304–307, <https://doi.org/10.1038/s41586-021-03907-3>.
- [3] Z.Y. Yu, Y. Duan, X.Y. Feng, X. Yu, M.R. Gao, S.H. Yu, Clean and affordable hydrogen fuel from alkaline water splitting: past, recent progress, and future prospects, *Adv. Mater.* 33 (2021), 2007100, <https://doi.org/10.1002/adma.202007100>.
- [4] J. Guan, X. Bai, T. Tang, Recent progress and prospect of carbon-free single-site catalysts for the hydrogen and oxygen evolution reactions, *Nano Res.* 15 (2021) 818–837, <https://doi.org/10.1007/s12274-021-3680-9>.
- [5] H. Jin, H. Yu, H. Li, K. Davey, T. Song, U. Paik, S.Z. Qiao, MXene analogue: a 2d nitridene solid solution for high-rate hydrogen production, *Angew. Chem. Int. Ed.* 61 (2022), e202203850, <https://doi.org/10.1002/anie.202203850>.
- [6] H. Jin, T. Song, U. Paik, S.-Z. Qiao, Metastable two-dimensional materials for electrocatalytic energy conversions, *Acc. Mater. Res.* 2 (2021) 559–573, <https://doi.org/10.1021/accountsmr.1c00115>.
- [7] X. Wang, D. Zhang, H. Zhang, L. Gong, Y. Yang, W. Zhao, S. Yu, Y. Yin, D. Sun, In situ polymerized polyaniline/MXene (V<sub>2</sub>C) as building blocks of supercapacitor and ammonia sensor self-powered by electromagnetic-triboelectric hybrid generator, *Nano Energy* 88 (2021) 2211–2855, <https://doi.org/10.1016/j.nanoen.2021.106242>.
- [8] T. Cui, X. Zhai, L. Guo, J.-Q. Chi, Y. Zhang, J. Zhu, X. Sun, L. Wang, Controllable synthesis of a self-assembled ultralow Ru, Ni-doped Fe<sub>2</sub>O<sub>3</sub> lily as a bifunctional electrocatalyst for large-current-density alkaline seawater electrolysis, *Chin. J. Catal.* 43 (2022) 2202–2211, [https://doi.org/10.1016/s1872-2067\(22\)64093-2](https://doi.org/10.1016/s1872-2067(22)64093-2).
- [9] H. Jin, X. Liu, A. Vasileff, Y. Jiao, Y. Zhao, Y. Zheng, S.Z. Qiao, Single-crystal nitrogen-rich two-dimensional moS<sub>2</sub> nanosheets for efficient and stable seawater splitting, *ACS Nano* 12 (2018) 12761–12769, <https://doi.org/10.1021/acsnano.8b07841>.
- [10] H. Jin, X. Wang, C. Tang, A. Vasileff, L. Li, A. Slattery, S.Z. Qiao, Stable and highly efficient hydrogen evolution from seawater enabled by an unsaturated nickel surface nitride, *Adv. Mater.* 33 (2021), e2007508, <https://doi.org/10.1002/adma.202007508>.
- [11] S. Li, L. Wang, H. Su, A.N. Hong, Y. Wang, H. Yang, L. Ge, W. Song, J. Liu, T. Ma, X. Bu, P. Feng, Electron redistributed s-doped nickel iron phosphides derived from one-step phosphatization of MOFs for significantly boosting electrochemical water splitting, *Adv. Funct. Mater.* 32 (2022), 2200733, <https://doi.org/10.1002/adfm.202200733>.
- [12] L. Yan, B. Zhang, J. Zhu, Y. Li, P. Tsiakaras, P. Kang Shen, Electronic modulation of cobalt phosphide nanosheet arrays via copper doping for highly efficient neutral-pH overall water splitting, *Appl. Catal. B Environ.* 265 (2020), 118555, <https://doi.org/10.1016/j.apcatb.2019.118555>.
- [13] C. Panda, P.W. Menezes, C. Walter, S. Yao, M.E. Miehlich, V. Gutkin, K. Meyer, M. Driess, From a molecular 2Fe-2Se precursor to a highly efficient iron diselenide electrocatalyst for overall water splitting, *Angew. Chem. Int. Ed.* 56 (2017) 10506–10510, <https://doi.org/10.1002/anie.201706196>.
- [14] W.H. Lai, L.F. Zhang, W.B. Hua, S. Indris, Z.C. Yan, Z. Hu, B. Zhang, Y. Liu, L. Wang, M. Liu, R. Liu, Y.X. Wang, J.Z. Wang, Z. Hu, H.K. Liu, S.L. Chou, S.X. Dou, General pi-electron-assisted strategy for Ir, Pt, Ru, Pd, Fe, Ni single-atom electrocatalysts with bifunctional active sites for highly efficient water splitting, *Angew. Chem. Int. Ed.* 58 (2019) 11868–11873, <https://doi.org/10.1002/anie.201904614>.
- [15] H. Sun, L. Chen, Y. Lian, W. Yang, L. Lin, Y. Chen, J. Xu, D. Wang, X. Yang, M. H. Rummerli, J. Guo, J. Zhong, Z. Deng, Y. Jiao, Y. Peng, S. Qiao, Topotactically transformed polygonal mesopores on ternary layered double hydroxides exposing under-coordinated metal centers for accelerated water dissociation, *Adv. Mater.* 32 (2020), 2006784, <https://doi.org/10.1002/adma.202006784>.
- [16] Y. Zhang, B. Zhou, Z. Wei, W. Zhou, D. Wang, J. Tian, T. Wang, S. Zhao, J. Liu, L. Tao, S. Wang, Coupling glucose-assisted Cu(I)/Cu(II) redox with electrochemical hydrogen production, *Adv. Mater.* 33 (2021), 2104791, <https://doi.org/10.1002/adma.202104791>.
- [17] L. Dai, Z.N. Chen, L. Li, P. Yin, Z. Liu, H. Zhang, Ultrathin Ni(0)-embedded Ni(OH)<sub>2</sub> heterostructured nanosheets with enhanced electrochemical overall water splitting, *Adv. Mater.* 32 (2020), 1906915, <https://doi.org/10.1002/adma.201906915>.
- [18] H. You, D. Wu, D. Si, M. Cao, F. Sun, H. Zhang, H. Wang, T.F. Liu, R. Cao, Monolayer NiIr-layered double hydroxide as a long-lived efficient oxygen evolution catalyst for seawater splitting, *J. Am. Chem. Soc.* 144 (2022) 9254–9263, <https://doi.org/10.1021/jacs.2c00242>.
- [19] Z. Duan, D. Zhao, Y. Sun, X. Tan, X. Wu, Bifunctional Fe-doped CoP@Ni<sub>2</sub>P heteroarchitectures for high-efficient water electrocatalysis, *Nano Res.* 15 (2022) 8865–8871, <https://doi.org/10.1007/s12274-022-4673-z>.
- [20] G. Li, H. Jang, S. Liu, Z. Li, M.G. Kim, Q. Qin, X. Liu, J. Cho, The synergistic effect of Hf-O-Ru bonds and oxygen vacancies in Ru/HfO<sub>2</sub> for enhanced hydrogen evolution, *Nat. Commun.* 13 (2022) 1270, <https://doi.org/10.1038/s41467-022-28947-9>.
- [21] T. Reier, Z. Pawolek, S. Cherevko, M. Bruns, T. Jones, D. Teschner, S. Selve, A. Bergmann, H.N. Nong, R. Schlögl, K.J. Mayrhofer, P. Strasser, Molecular insight in structure and activity of highly efficient, low-Ir Ni-Ni oxide catalysts for electrochemical water splitting (OER), *J. Am. Chem. Soc.* 137 (2015) 13031–13040, <https://doi.org/10.1021/jacs.5b07788>.
- [22] L. Bigiani, D. Barreca, A. Gasparotto, T. Andreu, J. Verbeeck, C. Sada, E. Modin, O. I. Lebedev, J.R. Morante, C. Maccato, Selective anodes for seawater splitting via functionalization of manganese oxides by a plasma-assisted process, *Appl. Catal. B Environ.* 284 (2021), 119684, <https://doi.org/10.1016/j.apcatb.2020.119684>.
- [23] S. Sultan, J.N. Tiwari, A.N. Singh, S. Zhumagali, M. Ha, C.W. Myung, P. Thangavel, K.S. Kim, Single atoms and clusters based nanomaterials for hydrogen evolution,

- oxygen evolution reactions, and full water splitting, *Adv. Energy Mater.* 9 (2019), 1900624, <https://doi.org/10.1002/aenm.201900624>.
- [24] X. Luo, P. Ji, P. Wang, R. Cheng, D. Chen, C. Lin, J. Zhang, J. He, Z. Shi, N. Li, S. Xiao, S. Mu, Interface engineering of hierarchical branched Mo-doped  $\text{Ni}_3\text{S}_2/\text{Ni}_3\text{P}_2$  hollow heterostructure nanorods for efficient overall water splitting, *Adv. Energy Mater.* 10 (2020), 1903891, <https://doi.org/10.1002/aenm.201903891>.
- [25] Y. Lin, K. Sun, X. Chen, C. Chen, Y. Pan, X. Li, J. Zhang, High-precision regulation synthesis of Fe-doped  $\text{Co}_2\text{P}$  nanorod bundles as efficient electrocatalysts for hydrogen evolution in all-pH range and seawater, *J. Energy Chem.* 55 (2021) 92–101, <https://doi.org/10.1016/j.jechem.2020.06.073>.
- [26] Y. Song, J. Cheng, J. Liu, Q. Ye, X. Gao, J. Lu, Y. Cheng, Modulating electronic structure of cobalt phosphide porous nanofiber by ruthenium and nickel dual doping for highly-efficiency overall water splitting at high current density, *Appl. Catal. B Environ.* 298 (2021), 120488, <https://doi.org/10.1016/j.apcatb.2021.120488>.
- [27] Q. Yu, J. Chi, G. Liu, X. Wang, X. Liu, Z. Li, Y. Deng, X. Wang, L. Wang, Dual-strategy of hetero-engineering and cation doping to boost energy-saving hydrogen production via hydrazine-assisted seawater electrolysis, *Sci. China Mater.* 65 (2022) 1539–1549, <https://doi.org/10.1007/s40843-021-1928-7>.
- [28] C.-F. Li, J.-W. Zhao, L.-J. Xie, J.-Q. Wu, G.-R. Li, Fe doping and oxygen vacancy modulated Fe- $\text{Ni}_3\text{P}_4/\text{NiFeOH}$  nanosheets as bifunctional electrocatalysts for efficient overall water splitting, *Appl. Catal. B Environ.* 291 (2021), 119987, <https://doi.org/10.1016/j.apcatb.2021.119987>.
- [29] Z. Wu, Y. Zhao, W. Jin, B. Jia, J. Wang, T. Ma, Recent progress of vacancy engineering for electrochemical energy conversion related applications, *Adv. Funct. Mater.* 31 (2020), 2009070, <https://doi.org/10.1002/adfm.202009070>.
- [30] Y. Yan, J. Lin, J. Cao, S. Guo, X. Zheng, J. Feng, J. Qi, Activating and optimizing the activity of NiCoP nanosheets for electrocatalytic alkaline water splitting through the V doping effect enhanced by P vacancies, *J. Mater. Chem. A* 7 (2019) 24486–24492, <https://doi.org/10.1039/c9ta09283h>.
- [31] G. Kresse, J. Furthmüller, Efficiency of ab-initio total energy calculations for metals and semiconductors using a plane-wave basis set, *Comput. Mater. Sci.* 6 (1996) 15–50, [https://doi.org/10.1016/0927-0256\(96\)00008-0](https://doi.org/10.1016/0927-0256(96)00008-0).
- [32] V. Wang, N. Xu, J.-C. Liu, G. Tang, W.-T. Geng, VASPKIT: a user-friendly interface facilitating high-throughput computing and analysis using VASP code, *Comput. Phys. Commun.* 267 (2021), 108033, <https://doi.org/10.1016/j.cpc.2021.108033>.
- [33] P.E. Blöchl, Projector augmented-wave method, *Phys. Rev. B* 50 (1994) 17953–17979, <https://doi.org/10.1103/PhysRevB.50.17953>.
- [34] J.P. Perdew, K. Burke, M. Ernzerhof, Generalized gradient approximation made simple, *Phys. Rev. Lett.* 77 (1996) 3865–3868, <https://doi.org/10.1103/PhysRevLett.77.3865>.
- [35] Z. Zhou, Y. Kong, H. Tan, Q. Huang, C. Wang, Z. Pei, H. Wang, Y. Liu, Y. Wang, S. Li, X. Liao, W. Yan, S. Zhao, Cation-vacancy-enriched nickel phosphide for efficient electrosynthesis of hydrogen peroxides, *Adv. Mater.* 34 (2022), 2106541, <https://doi.org/10.1002/adma.202106541>.
- [36] R. Xu, T. Jiang, Z. Fu, N. Cheng, X. Zhang, K. Zhu, H. Xue, W. Wang, J. Tian, P. Chen, Ion-exchange controlled surface engineering of cobalt phosphide nanowires for enhanced hydrogen evolution, *Nano Energy* 78 (2020) 2211–2855, <https://doi.org/10.1016/j.nanoen.2020.105347>.
- [37] X. Zhang, L. Song, L. Tong, M. Zeng, Y. Wang, Surface bonding of CoP to biomass derived carbon microtube: site-specific growth and high-efficiency catalysis, *Chem. Eng. J.* 440 (2022), 135884, <https://doi.org/10.1016/j.cej.2022.135884>.
- [38] Y. Zhao, B. Jin, Y. Zheng, H. Jin, Y. Jiao, S.Z. Qiao, Charge state manipulation of cobalt selenide catalyst for overall seawater electrolysis, *Adv. Energy Mater.* 8 (2018), 1801926, <https://doi.org/10.1002/aenm.201801926>.
- [39] A. Serov, K. Artyushkova, P. Atanassov, Fe-N-C oxygen reduction fuel cell catalyst derived from carbendazim: synthesis, structure, and reactivity, *Adv. Energy Mater.* 4 (2014), 1301735, <https://doi.org/10.1002/aenm.201301735>.
- [40] Y.W. Li, W.J. Zhang, J. Li, H.Y. Ma, H.M. Du, D.C. Li, S.N. Wang, J.S. Zhao, J. M. Dou, L. Xu, Fe-MOF-derived efficient ORR/OER bifunctional electrocatalyst for rechargeable zinc-air batteries, *ACS Appl. Mater. Interfaces* 12 (2020) 44710–44719, <https://doi.org/10.1021/acsami.0c11945>.
- [41] L. Wu, L. Yu, F. Zhang, B. McElhenny, D. Luo, A. Karim, S. Chen, Z. Ren, Heterogeneous bimetallic phosphide  $\text{Ni}_3\text{P-Fe}_2\text{P}$  as an efficient bifunctional catalyst for water/seawater splitting, *Adv. Funct. Mater.* 31 (2020), 2006484, <https://doi.org/10.1002/adfm.202006484>.
- [42] W. Li, Y. Jiang, Y. Li, Q. Gao, W. Shen, Y. Jiang, R. He, M. Li, Electronic modulation of CoP nanoarrays by Cr-doping for efficient overall water splitting, *Chem. Eng. J.* 425 (2021), <https://doi.org/10.1016/j.cej.2021.130651>.
- [43] F. Ma, Q. Wu, M. Liu, L. Zheng, F. Tong, Z. Wang, P. Wang, Y. Liu, H. Cheng, Y. Dai, Z. Zheng, Y. Fan, B. Huang, Surface fluorination engineering of NiFe Prussian Blue analogue derivatives for highly efficient oxygen evolution reaction, *ACS Appl. Mater. Interfaces* 13 (2021) 5142–5152, <https://doi.org/10.1021/acsami.0c20886>.
- [44] F. Yang, Y. Luo, Q. Yu, Z. Zhang, S. Zhang, Z. Liu, W. Ren, H.M. Cheng, J. Li, B. Liu, A durable and efficient electrocatalyst for saline water splitting with current density exceeding  $2000 \text{ mA cm}^{-2}$ , *Adv. Funct. Mater.* 31 (2021), 2010367, <https://doi.org/10.1002/adfm.202010367>.
- [45] G. Yang, Y. Jiao, H. Yan, Y. Xie, A. Wu, X. Dong, D. Guo, C. Tian, H. Fu, Interfacial engineering of  $\text{MoO}_3\text{-FeP}$  heterojunction for highly efficient hydrogen evolution coupled with biomass electrooxidation, *Adv. Mater.* 32 (2020), 2000455, <https://doi.org/10.1002/adma.202000455>.
- [46] R. Zhang, J. Huang, G. Chen, W. Chen, C. Song, C. Li, K. Ostrikov, In situ engineering bi-metallic phospho-nitride bi-functional electrocatalysts for overall water splitting, *Appl. Catal. B Environ.* 254 (2019) 414–423, <https://doi.org/10.1016/j.apcatb.2019.04.089>.
- [47] X. Yuan, H. Ge, X. Wang, C. Dong, W. Dong, M.S. Riaz, Z. Xu, J. Zhang, F. Huang, Controlled phase evolution from Co nanochains to CoO nanocubes and their application as OER catalysts, *ACS Energy Lett.* 2 (2017) 1208–1213, <https://doi.org/10.1021/acsenenergylett.7b00223>.
- [48] Q. Xu, H. Jiang, X. Duan, Z. Jiang, Y. Hu, S.W. Boettcher, W. Zhang, S. Guo, C. Li, Fluorination-enabled reconstruction of NiFe electrocatalysts for efficient water oxidation, *Nano Lett.* 21 (2021) 492–499, <https://doi.org/10.1021/acs.nanolett.0c03950>.
- [49] X. Xu, T. Guo, J. Xia, B. Zhao, G. Su, H. Wang, M. Huang, A. Toghan, Modulation of the crystalline/amorphous interface engineering on Ni-P-O-based catalysts for boosting urea electrolysis at large current densities, *Chem. Eng. J.* 425 (2021) 1385–8947, <https://doi.org/10.1016/j.cej.2021.130514>.
- [50] Y. Cheng, X. Yang, M. Li, X. Li, X. Lu, D. Wu, B. Han, Q. Zhang, Y. Zhu, M. Gu, Enabling ultrastable alkali metal anodes by artificial solid electrolyte interphase fluorination, *Nano Lett.* 22 (2022) 4347–4353, <https://doi.org/10.1021/acs.nanolett.2c00616>.
- [51] X. Gu, Z. Liu, H. Liu, C. Pei, L. Feng, Fluorination of ZIF-67 framework templated Prussian blue analogue nano-box for efficient electrochemical oxygen evolution reaction, *Chem. Eng. J.* 403 (2021), 126371, <https://doi.org/10.1016/j.cej.2020.126371>.
- [52] Y. Zhu, H.-C. Chen, C.-S. Hsu, T.-S. Lin, C.-J. Chang, S.-C. Chang, L.-D. Tsai, H. M. Chen, Operando unraveling of the structural and chemical stability of P-substituted  $\text{CoSe}_2$  electrocatalysts toward hydrogen and oxygen evolution reactions in alkaline electrolyte, *ACS Energy Lett.* 4 (2019) 987–994, <https://doi.org/10.1021/acsenenergylett.9b00382>.
- [53] J. Duan, S. Chen, C.A. Ortiz-Ledon, M. Jaroniec, S.Z. Qiao, Phosphorus vacancies that boost electrocatalytic hydrogen evolution by two orders of magnitude, *Angew. Chem. Int. Ed.* 59 (2020) 8181–8186, <https://doi.org/10.1002/anie.201914967>.
- [54] J. Teng, X. Qin, W. Guo, X. Song, S. Xiao, Y. Min, Q. Xu, J. Fan, Boron nitride quantum dots coupled with CoP nanosheet arrays grown on carbon cloth for efficient nitrogen reduction reaction, *Chem. Eng. J.* 440 (2022) 1385–8947, <https://doi.org/10.1016/j.cej.2022.135853>.
- [55] J.C. Kim, D.W. Kim, Enhanced hydrogen evolution activities of the hollow surface-oxidized cobalt phosphide nanofiber electrocatalysts in alkaline media, *Int. J. Energy Res.* 46 (2022) 13035–13043, <https://doi.org/10.1002/er.7973>.
- [56] J. Ren, N. Jiang, K. Shang, N. Lu, J. Li, Y. Wu, Synergistic degradation of trans-ferric acid by water falling film DBD plasma coupled with cobalt oxyhydroxide: performance and mechanisms, *Chem. Eng. J.* 372 (2019) 321–331, <https://doi.org/10.1016/j.cej.2019.04.147>.
- [57] S. Seenivasan, J. Seo, Inverting destructive electrochemical reconstruction of niobium nitride catalyst to construct highly efficient HER/OER catalyst, *Chem. Eng. J.* 454 (2023) 1385–8947, <https://doi.org/10.1016/j.cej.2022.140558>.
- [58] S. Anantharaj, S. Kundu, S. Noda, “The Fe Effect”: a review unveiling the critical roles of Fe in enhancing OER activity of Ni and Co based catalysts, *Nano Energy* 80 (2021) 2211–2855, <https://doi.org/10.1016/j.nanoen.2020.105514>.